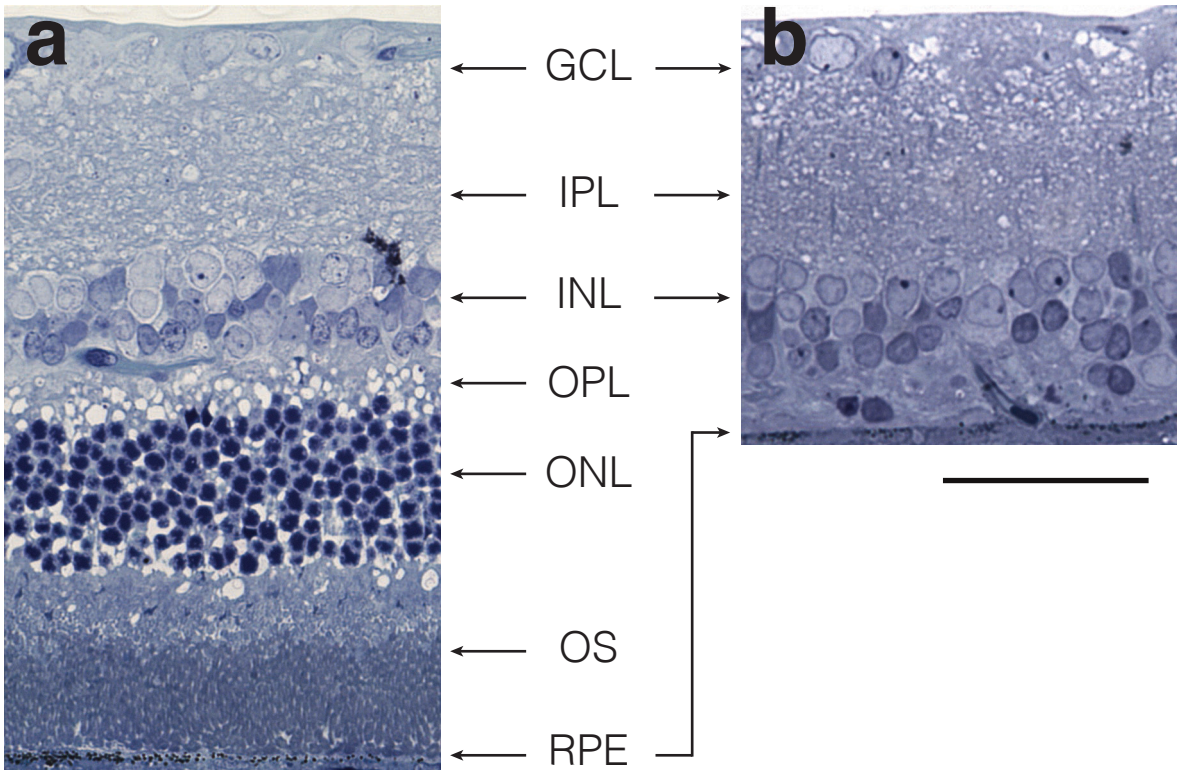

Supplementary Figure 1: **Histological comparison of healthy and degenerate rat retina.** (**a**) Histological cross-section of a healthy rat retina. Photoreceptor outer segments (OS) are in contact with the retinal pigment epithelium (RPE). Photoreceptor somas located in the outer nuclear layer (ONL) transmit neural signals to cells in the inner nuclear layer (INL) via synapses located in the outer plexiform layer (OPL). From there, signals are relayed to the ganglion cell layer (GCL) via synapses in the inner plexiform layer (IPL). (**b**) Histological cross-section of a P140 RCS rat retina. The OS, ONL and OPL have degenerated and the INL is now in contact with the RPE. The INL, IPL and GCL are preserved to a large extent. Scale bar: 50 μm.

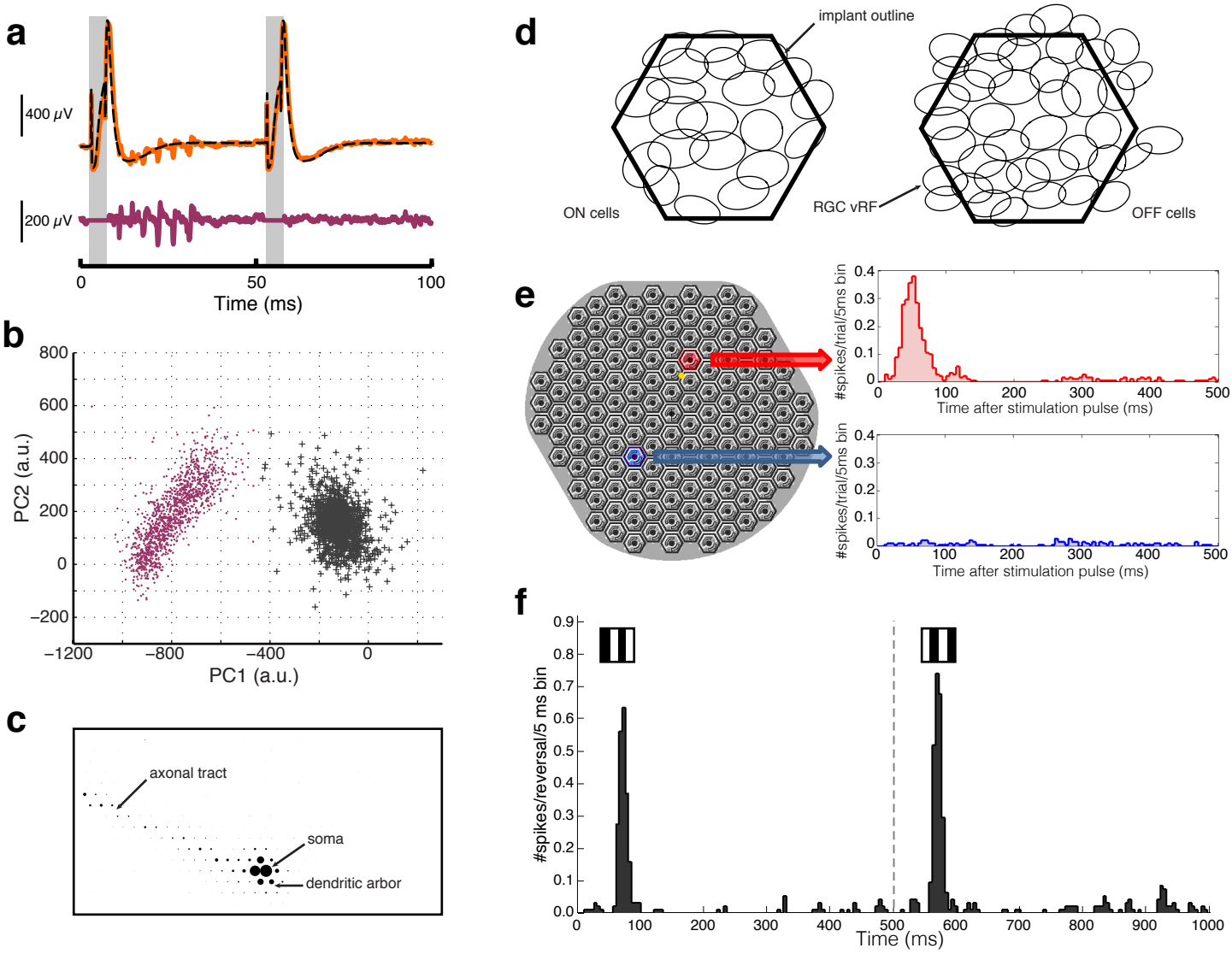

Supplementary Figure 2: **Data processing.** (**a**) We estimated electrical stimulation artifacts by averaging over many trials (black dashed trace), aligning and pointwise subtracting from the raw recordings (orange). Artifact removal is often imperfect over the duration of the light pulse (shaded) therefore we blanked data in software, resulting in the purple trace. Action potentials are subsequently detected by thresholding prior to (**b**) undergoing principal component analysis (PCA) and expectation-maximization clustering. (**c**) Putative neural activity is correlated with the recorded electrical activity over the implant, thereby creating electrophysiological images (EIs) of the ganglion cells. Triangulation of this voltage signature localizes RGCs over the recording array. We discarded from the analysis cells exhibiting abnormal EIs, indicative of improper spike sorting (for example, RGCs with multiple axons). (**d**) Finally, we correlated the firing patterns with the stimulus. White noise analysis shows receptive field mosaics underneath the implant for both ON and OFF cells, an indicator that the retina was in good physiological condition. (**e**) For eRF mapping, we recorded responses from each RGC (yellow dot) to each pixel stimulation. (**f**) For alternating grating measurements, spiking patterns are correlated with the grating contrast reversal. The peristimulus time histogram shown here exhibits response to both phases of the grating, characteristic of non-linear summation in subunits of the RGC receptive field.

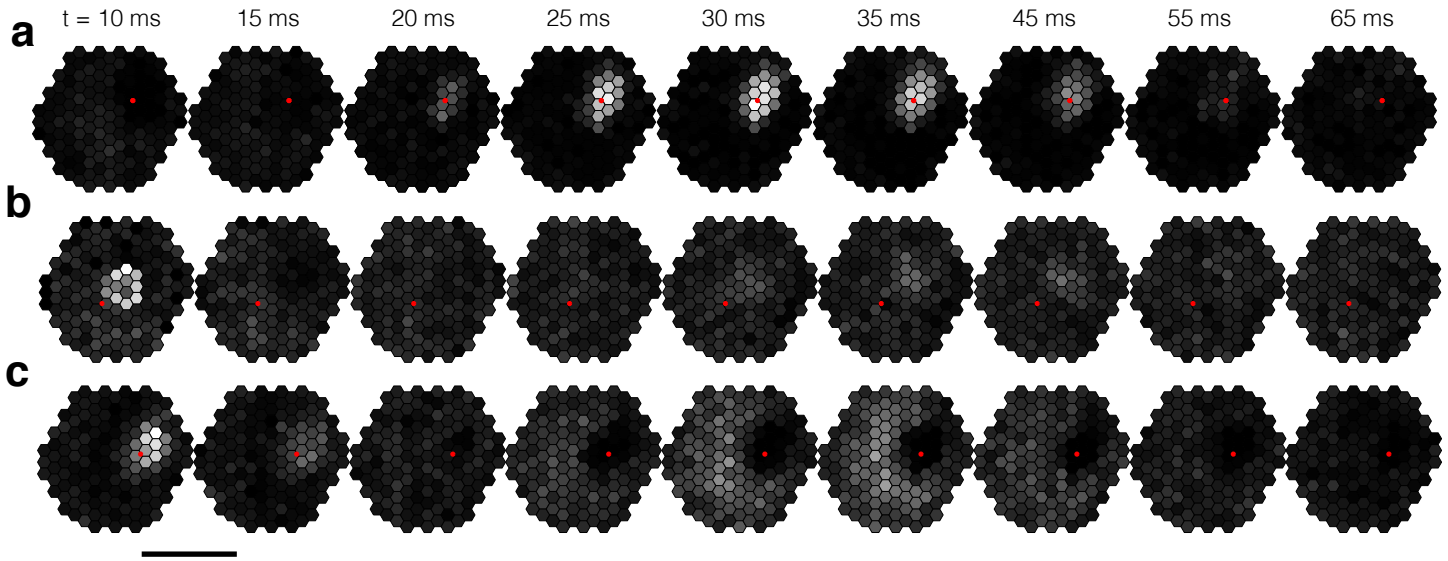

Supplementary Figure 3: **Time course of the eRFs.** (**a**) The most commonly observed type of eRF had a localized component with latency 20 – 45 ms. (**b**) Some eRFs had a localized component with a shorter (< 15 ms) latency. (**c**) For eRFs with center and diffuse components, the central localized response had a short latency (< 15 ms), and the diffuse latency was 20-45 ms. In all figures, the red dot indicates the estimated position of the RGC soma on the array (see Supplementary Fig 2c). Scale bar: 500 μm.

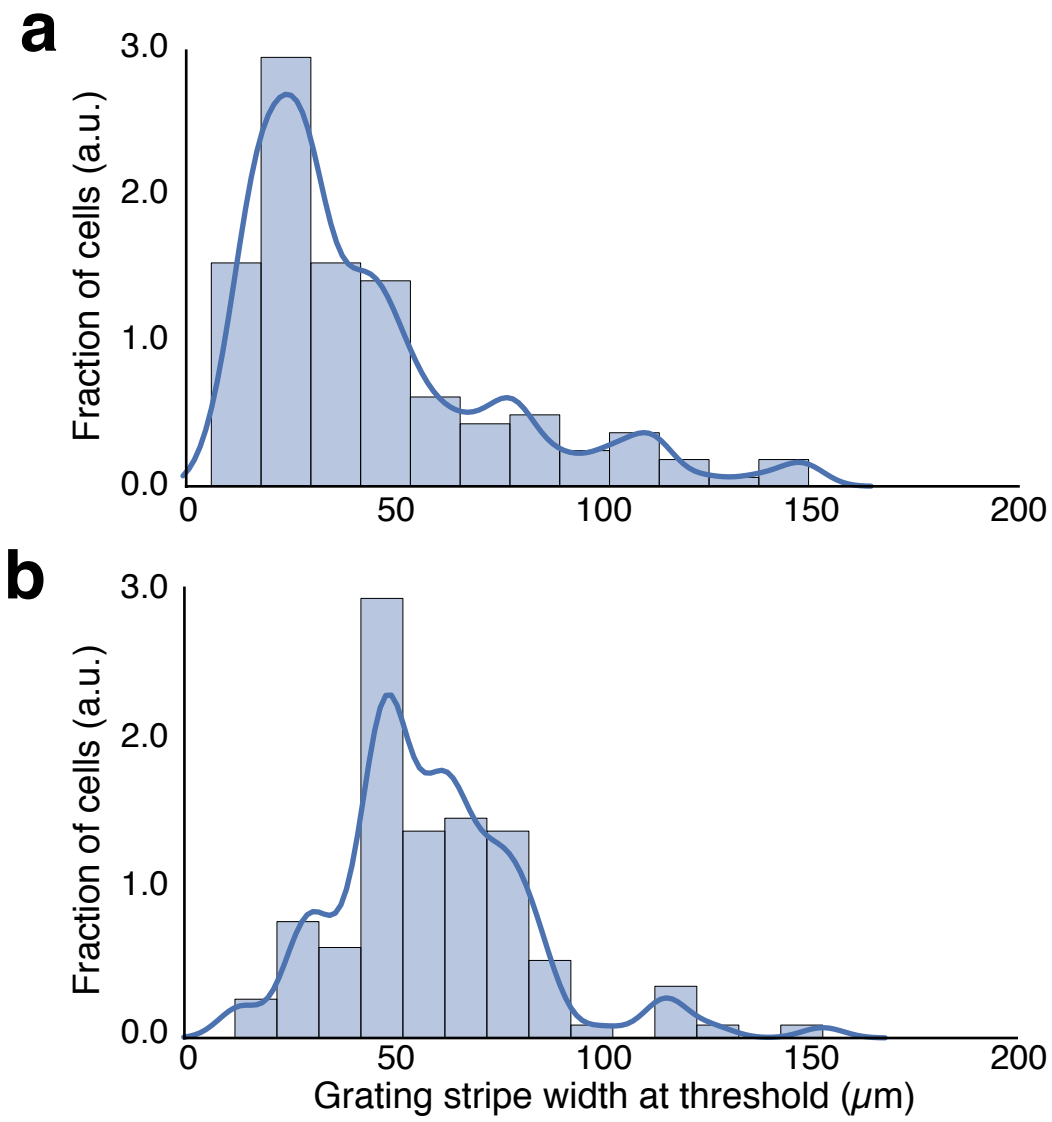

Supplementary Figure 4: **Distribution of the responses to alternating gratings projected with visible light.** Histograms and kernel density estimates of the stimulation thresholds for alternating gratings in two different preparations. (**a**) The peak in the threshold distribution occurs at 28 μm (n = 163 RGCs). (**b**) The peak in the threshold distribution occurs at 48 μm (n = 115 RGCs).

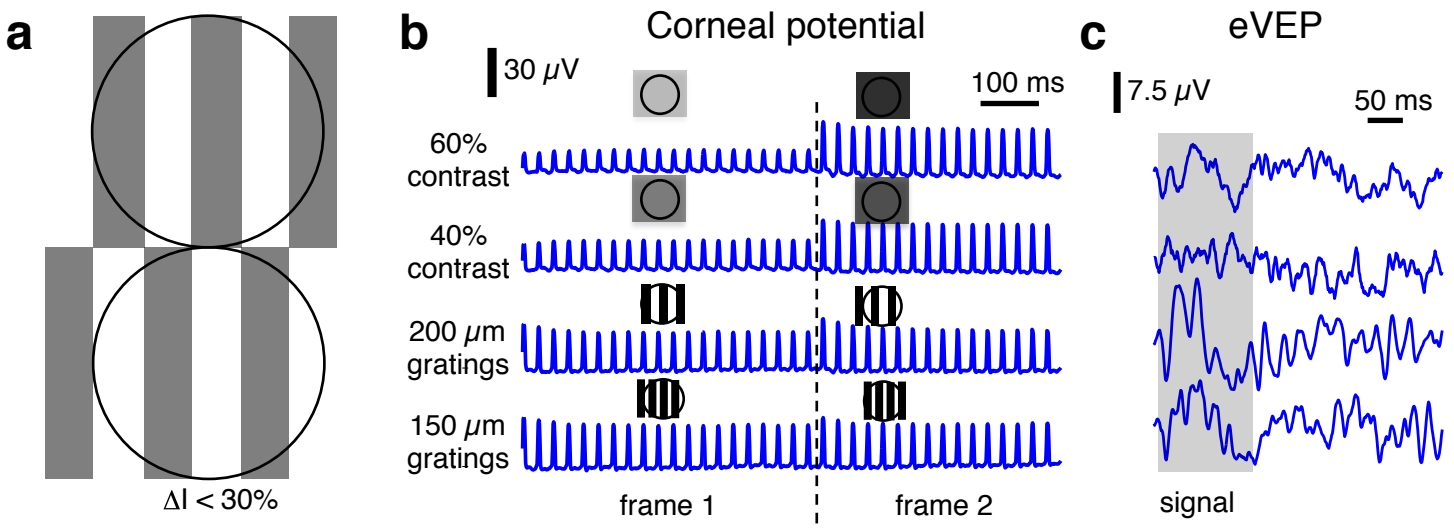

Supplementary Figure 5: **Responses to grating alternations are not due to a luminance misbalance.** (**a**) Illustration of the two phases of the large gratings overlapping with the implant. The total stimulation current was assessed via a corneal electrode, thereby comparing the stimulus misbalance (ΔI) between the two phases (**b**) In all conditions, even with the large gratings, this misbalance was below 30%. To verify whether this change in the total current could elicit responses to the alternating gratings, we recorded the VEP responses to full-field stimulation with contrast modulation (**c**) Animals responded to 60% contrast, but did not respond to 40% contrast. Therefore, strong responses to the gratings with 200 μm and narrower stripes could not be due to the luminance misbalance, but rather originate from the spatial modulation of the stimulus.

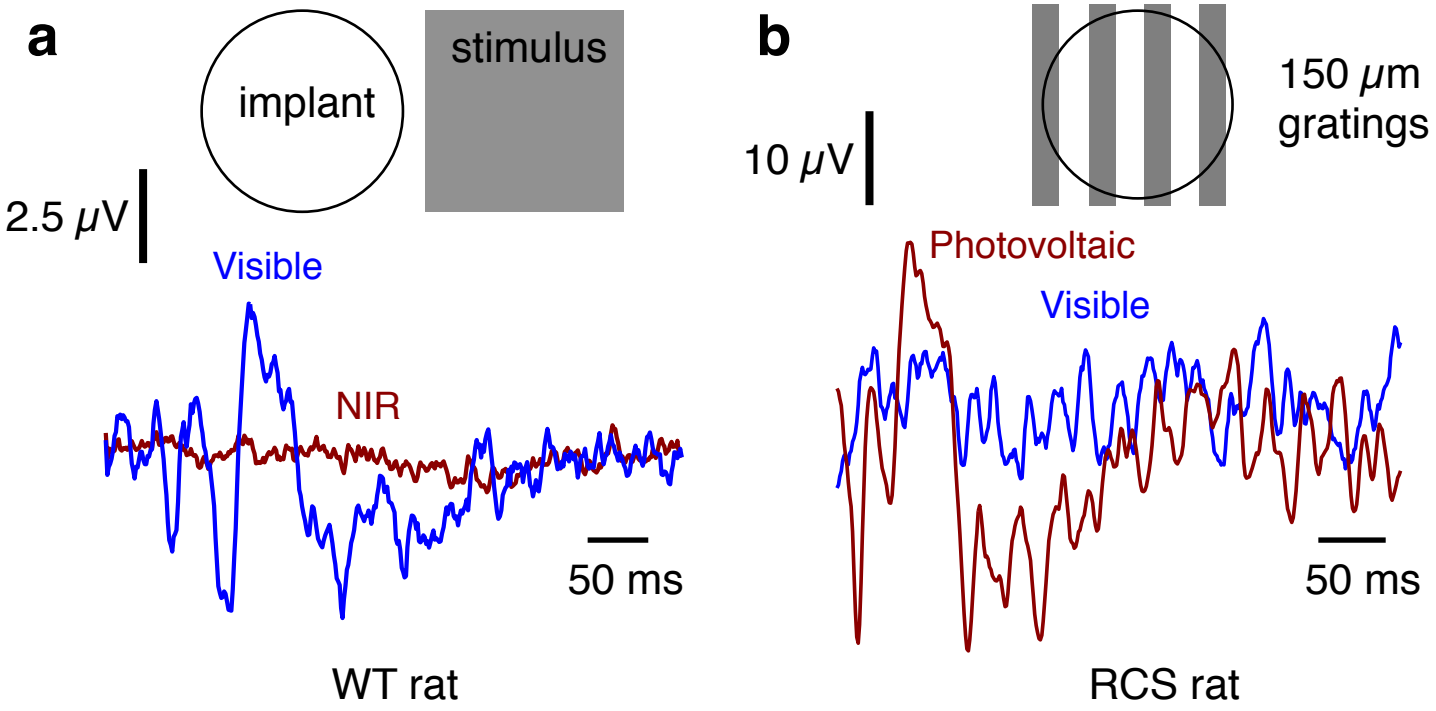

Supplementary Figure 6: **Control experiments.** (**a**) Lack of VEP responses to NIR stimulation outside of the implant (red) and a strong response to the visible light in the same location in a WT animal (blue). (**b**) Lack of VEP response to alternating grating with 150 μm/stripe projected with visible light onto the implant in RCS rat (blue) and a robust response to patterns projected with NIR illumination (red).

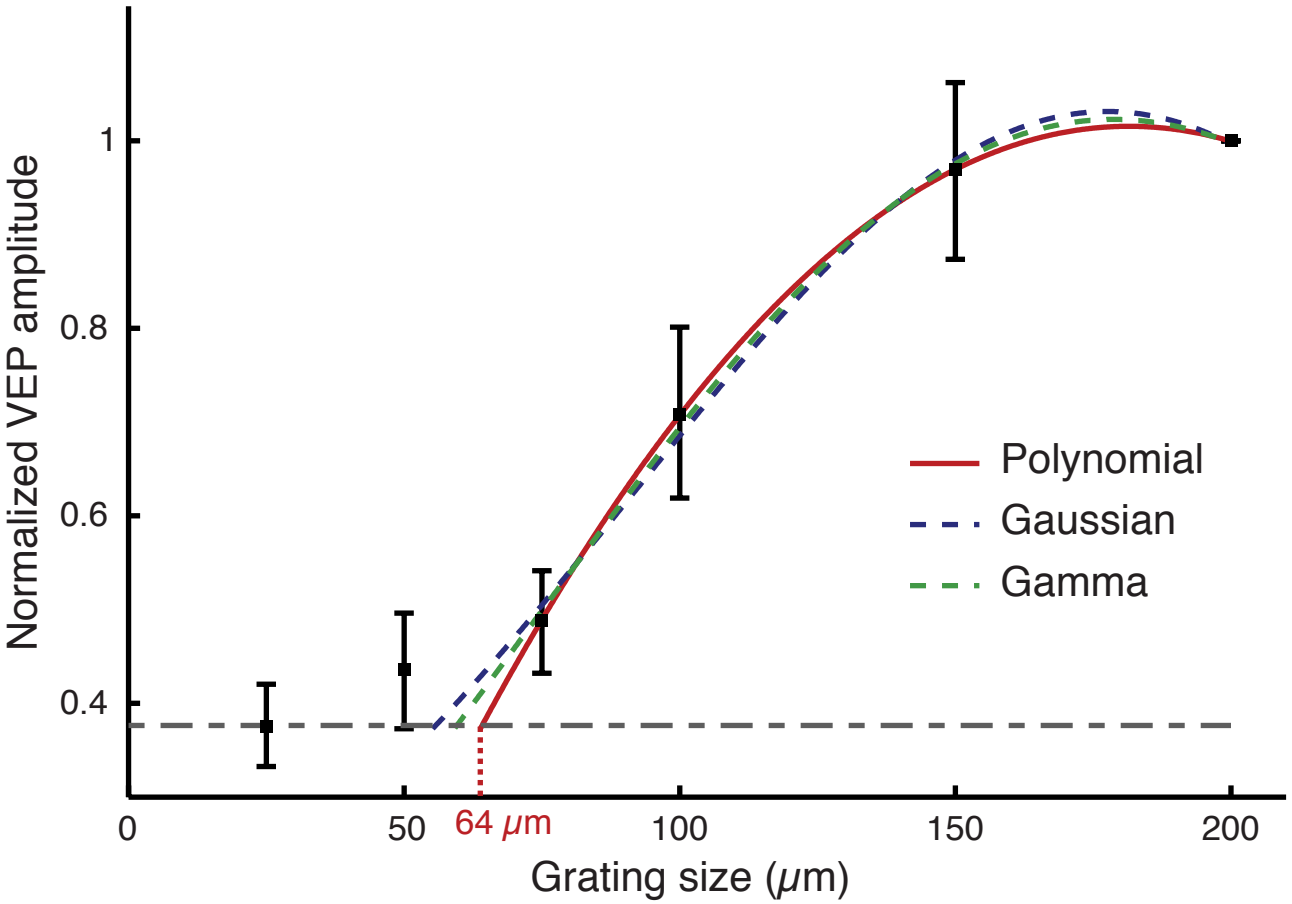

Supplementary Figure 7: **Visual acuity estimation.** We obtained the acuity value by calculating the intersection of a fit of the data points and the noise level. For prosthetic visual acuity, we used 75, 100, 150 and 200 μm data points. We defined the noise level as the amplitude of the signal in response to alternations of the grating with 25µm/stripe, which are not resolved. A second order polynomial fitting yielded the most conservative estimate of the acuity among the different functions tested (sigmoidal, Gaussian and polynomial, see Methods). We calculated the uncertainty of the measurement from the fitting parameter covariance and the uncertainty in the noise level (see Methods).

Type	WT	RCS
Receptive fields	$n = 4$, 92 cells	$n = 3$, 48 cells
In vitro gratings	$n = 2$, 278 cells	$n = 4$, 109 cells
In vitro frequency	$n = 2$, 178 cells	$n = 2$, 45 cells
In-vivo full field	$n = 9$	$n = 3$
In-vivo acuity	$n = 7$	$n = 7$

Table 1: **Data summary.** Number of cells and animals contributing to each experiment.